Modeling phase equilibrium of hydrogen and natural gas in brines: Application to storage in salt caverns

Juan Sebastian Roa Pinto, Pierre Bachaud, Tiphaine Fargetton, Nicolas Ferrando, Laurent Jeannin, Floriane Louvet

Modeling phase equilibrium of hydrogen and natural gas in brines: Application to storage in salt caverns

Juan Sebastian Roa Pinto[1,2], Pierre Bachaud[1], Tiphaine Fargetton[2], Nicolas Ferrando[1,*], Laurent Jeannin[2], Floriane Louvet[2]

[1] IFP Energies nouvelles, 1 et 4 avenue de Bois-Preau, 92850 Rueil-Malmaison Cedex, France
[2] STORENGY, 12 rue Raoul Nordling, 92270 Bois-Colombes, France

ABSTRACT

In this work, the e-PPC-SAFT equation of state has been parameterized to predict phase equilibrium of the system H_2 + CH_4 + H_2O + Na^+Cl^- in conditions of temperature, pressure and salinities of interest for gas storage in salt caverns. The ions parameters have been adjusted to match salted water properties such as mean ionic coefficient activities, vapor pressures and molar densities. Furthermore, binary interaction parameters between hydrogen, methane, water, Na^+ and Cl^- have been adjusted to match gas solubility data through Henry constant data. The validity ranges of this model are 0 to 200 °C for temperatures, 0 to 300 bar for pressures, and 0 to 8 mol_{NaCl}/kg_{H2O} for salinities. The e-PPC-SAFT equation of state has then been used to model gas storage in salt caverns. The performance of a storage of pure methane, pure hydrogen and a mixture methane + hydrogen have been compared. The simulations of the storage cycles show that integrating up to 20% of hydrogen in caverns does not have a major influence on temperature, pressure and water content compared to pure methane storage. They also allowed to estimate the thermodynamic properties of the system during the storage operations, like the water content in the gaseous phase. The developed model constitutes thus an interesting tool to help size surface installations and to operate caverns.

Keywords: Hydrogen ; thermodynamic model ; phase equilibrium ; natural gas ; cavern storage

* Corresponding author: Email: nicolas.ferrando@ifpen.fr. Phone: +33 1 47 52 66 24.

1 Introduction

Underground storage in salt caverns is a well-known technique for natural gas, which ensures flexibility on the gas network and supplies security during the winter season. These caverns behave as pressure vessels and may deliver high flow rates on demand. Evolution of the natural gas market in the last few years has changed the way caverns are operated. They are used in more and more aggressive modes, with shorter cycles. In this context, it becomes very important to predict moisture content at the wellhead and in the cavern, in order to design the surface units and optimize exploitation. In addition, a new challenge for operators is emerging with hydrogen storage. Indeed, the valorization of electricity produced during periods of low consumption from renewable sources, such as solar photovoltaic or wind, is one of the challenges of the energy transition from fossil fuels. A possible option consists in converting this excess electricity into hydrogen by water electrolysis [1]. The hydrogen produced by this power-to-gas process can then either be injected, up to few percents, in the natural gas network [2,3] and stored in geological formations, or be stored pure in geological formations [4–6]. For the latter option, salt caverns present several advantages for massive storage of hydrogen as a pure product [7–10], notably the very low permeability of salt layers and the flexibility allowed by these structures, compatible with the variable production and usages associated with hydrogen.

Salt caverns are built by leaching: rock salt is dissolved by injecting water underground, causing the production of brine. After the leaching phase gas is injected in order to remove as much brine as possible from the salt cavern, this is the first filling (or de-brining) phase. A significant amount of brine remains at the bottom of the cavern after the de-brining phase. Operations of storage start thereafter: gas injection and withdrawal vary according to customer needs, and cause compression or expansion of the gas in the cavern. Gas is injected at a prescribed flow rate and temperature at the wellhead, and is withdrawn at a given flow rate. Inside the cavern and the well, gas exchanges heat with the surrounding rock, inducing temperature and pressure variations. In the cavern, gas pressure has to remain between a minimum (to limit salt creeping) and a maximum value (set far below the lithostatic pressure to avoid any mechanical damages). During the operations, water evaporates in the gas, while gaseous components dissolve in the brine. For a natural gas storage, the former may be very limiting: if moisture content in the gas is too high, hydrates could form during withdrawal in the upper part of the well [11,12]. In the case of hydrogen, depending on the usage planned after production, a high purity might be required. This will impose the use of dehydration units. On the other hand, evaluation of gas loss by dissolution may be interesting for operators considering mechanical integrity tests (cavern in that case is partially filled) or during de-brining phases. It is thus of primary importance for operators to dispose of a thermodynamic model able to accurately predict the temperature, pressure and phases composition at wellhead and inside the cavern to correctly dimension surface facilities during the phase of preliminary design, and to determine the storage performance and improve its exploitation during operations [11–13].

During the three last decades, many thermodynamic models have been developed to predict phase equilibrium of methane (or natural gas) in brines, including activity coefficient models (*e.g.* [14–16]) or equations of state (*e.g.* [17–25]). However, only very few models have been published for phase equilibrium of hydrogen in brines [26–28]. This is probably due to the lack of available experimental data in the operating conditions of industrial applications [29]. Therefore, it is necessary to focus on a predictive thermodynamic model to be able to extrapolate in conditions of caverns operation.

In this paper, the e-PPC-SAFT (electrolyte-Polar Perturbed-Chain Statistical Association Fluid Theory) equation of state (EoS) is used for modeling the vapor-liquid equilibria of the systems H_2O + NaCl + H_2 + CH_4 for thermodynamic conditions met in salt caverns. This model is an extension of the original

PC-SAFT EoS [30] to polar and electrolytic systems [24]. The SAFT equation is based on statistical thermodynamics and allows the thermodynamic characterization of a fluid by incorporating the effects of association. One of the main advantage of the SAFT theory is that it relies on a realistic physical representation of the molecules taking into account their shape, their size, as well as the different interactions that may exist between the molecules of a fluid. Moreover the SAFT equation can represent very different types of fluids (electrolyte solution, polar solvents, hydrogen-bonded fluids) and is more accurate to predict phase densities (or, in other word, the compressibility factor) than the usual cubic state equations. This study proposed a parameterization of the e-PPC-SAFT EoS based on the available experimental data for both systems.

This paper is organized as follows. First, the formalism description of the e-PPC-SAFT model is shown. Then, pure components, brine and gas+brine mixtures (H_2 + CH_4 + H_2O + Na^+Cl^-) will be studied in order to find the parameters that accurately describe the phase equilibrium for a range of salt concentrations between 0 mol/kg_{H2O} and 8 mol/kg_{H2O}, as well as pressures between 0 bar and 300 bar and temperatures between 0 and 200 °C. Finally, this thermodynamic model will be implemented in a numerical model of salt cavern storage and applied [31] to study synthetic cases of storage of pure methane, pure hydrogen and a mixture of this two gases in order to quantify the storage performances.

2 Thermodynamic model

2.1 The e-PPC-SAFT equation of state

The e-PPC-SAFT equation of state computes the residual Helmholtz energy of a system by the addition of various terms, each term describing specific physical interactions between molecules in this system:

$$\frac{A^{res}}{RT} = \frac{A^{HS}}{RT} + \frac{A^{chain}}{RT} + \frac{A^{disp}}{RT} + \frac{A^{assoc}}{RT} + \frac{A^{polar}}{RT} + \frac{A^{NAHS}}{RT} + \frac{A^{MSA}}{RT} + \frac{A^{Born}}{RT} \quad (1)$$

The mathematical expression of each of these terms are well described in the literature [24,30,32,33] and are therefore not recalled in this work. Only a brief summary of the physical meaning of these terms and the corresponding pure component and binary parameters used in this work are provided in Table 1.

Table 1. The different terms of the e-PPC-SAFT equation of state and their pure component and binary parameters.

Term	Physical meaning	Pure component parameters	Binary parameters
A^{HS}	Repulsive energy between hard spheres	σ_i^{HS} (segment diameter)	-
A^{chain}	Chain formation energy between segments	m_i (segment numbers)	-
A^{disp}	Dispersive energy between spheres	ε_i (dispersion energy)	k_{ij}
A^{assoc}	Association energy between segments	ε^{AB} (association energy) k^{AB} (association volume)	-
A^{polar}	Energy between polar moments	μ_i (dipole moment) χ_{pi} (dipole fraction)	-
A^{NAHS}	Non-additive hard sphere energy	-	l_{ij}
A^{MSA}	Long-range electrostatic interactions between ions (MSA theory)	σ_i^{MSA}	-
A^{Born}	Born energy for ions (solvation)	σ_i^{Born}	-

From the derivatives of the residual Helmholtz energy with respect to pressure, temperature and mole numbers, it is possible to determine all the thermodynamic properties of the system such as compressibility factors, molar volumes, residual heat capacities, Joule-Thomson coefficients, and, more specifically, the fugacity coefficient of the i^{th} component in the phase p (φ_i^p) defined as:

$$RT\ln\varphi_i^p = \left(\frac{\partial A^{res,p}(T,V)}{\partial n_i}\right)_{T,V^p,n_{j\neq i}} - RT\ln\frac{Pv^p}{RT} \qquad (2)$$

where *T* is the temperature, *V* the volume, *P* the pressure, *R* is the ideal gas constant, n_i the number of mole of the i^{th} component and *v* the molar volume of the phase *p*.

The fugacity coefficient is a key-property to compute liquid-vapor phase equilibrium, which is obtained by equalizing the fugacity in the liquid and vapor phases for each component under the mass balance constraint:

$$Px_i\varphi_i^{liq}\left(T,P,\overline{x}\right) = Py_i\varphi_i^{vap}\left(T,P,\overline{y}\right) \qquad (3)$$

where x_i and y_i are the molar fractions of the component *i* in the liquid and vapor phase respectively, $\overline{x}$ and $\overline{y}$ the vectors of composition of the liquid and vapor phase, and φ_i^{liq} and φ_i^{vap} the fugacity coefficients of the i^{th} component in the liquid and vapor phase.

In the thermodynamic conditions considered here, the solubility of a light gas in water is very low. It is thus common to measure and model this quantity in term of Henry constant H_i, which can be directly determined from the fugacity coefficient by:

$$H_i = P_s^{\sigma}(T)\cdot\varphi_i^{liq,\infty}\left(T,P,\overline{x}\right) \qquad (4)$$

where P_s^{σ} is the saturation pressure of the solvent, and $\varphi_i^{liq,\infty}$ the liquid fugacity coefficient of the solute *i* at infinite dilution ($x_i \rightarrow 0$).

In the various contributions to the total residual Helmholtz energy, the terms A^{MSA} (long-range electrostatic interactions) and A^{Born} (ions solvation energy) are directly related to ionic species, and are of primary importance for modeling thermodynamic properties and phase equilibrium in highly salted solutions, such as brines in salt caverns. As shown in Table 1, it can be noticed that these two terms involve a specific ion diameter σ_i^{MSA} and σ_i^{Born}, which can be seen as a "solvated" ion diameter and are consequently expected to be larger than ion hard sphere diameter σ_i^{HS} [34]. In order to ensure this physical consistency, we propose to introduce in this work a proportionality coefficient **λ** defined by:

$$\sigma_i^{MSA} = \lambda^{MSA}\sigma_i^{HS} \qquad (5)$$

$$\sigma_i^{Born} = \lambda^{Born}\sigma_i^{HS} \qquad (6)$$

Both MSA and Born energies are strongly driven by the dielectric constant *D* of the solution. In the e-PPC-SAFT framework, the salt-concentration dependence proposed by Simonin [35] is used to model this property:

$$D = \frac{D_w}{1+\sum_{ion}\alpha x_{ion}} \qquad (7)$$

where **α** is an adjustable parameter, x_{ion} the molar fraction of the ions in the solution, and D_w the dielectric constant of pure water taken from Schrekenberg *et al.* [36]:

$$D_w = 1 + \frac{0.0003777}{\rho}\left(\frac{1403}{T} - 1\right) \qquad (8)$$

ρ is the molar density of pure water.

In order to obtain better accuracy on a large range of temperatures, the α parameter is assumed temperature-dependent:

$$\alpha = \alpha_0 + \alpha_1 (T - 298.15) \qquad (9)$$

where α_0 and α_1 are constants.

A common property used to characterize the non-ideality in electrolyte solutions is the mean ionic activity coefficient (MIAC), defined by the average of the activity coefficient of the individual ions constituting the considered salt. For an NaCl aqueous solution, it is thus defined by:

$$\gamma_{MIAC} = \left(\gamma_{Na^+}\gamma_{Cl^-}\right)^{1/2} \qquad (10)$$

The individual ionic activity coefficients can be calculated from their fugacity coefficients, using the relationship:

$$\gamma_i = \frac{\varphi_i^{liq}(T, P, x_i)}{\varphi_i^{liq,\infty}(T, P, x_i \to 0)} \qquad (11)$$

2.2 Pure component parameters

2.2.1 Hydrogen and methane

The e-PPC-SAFT parameters of pure hydrogen and pure methane are taken from literature [37,38] and are recalled in Table 2. For gas storage in salt caverns application, two thermodynamic properties are of primary importance to correctly simulate the gas injection-removal cycles: the density of the vapor phase (or, similarly, its compressibility factor *Z*), and the Joule-Thomson coefficient, which quantifies the variation of temperature during a pressure change. It is thus necessary to validate the choice of the pure component parameters of hydrogen and methane on both these properties. As stated below, the phase density and compressibility factor are directly given by the equation of state. The Joule-Thomson coefficient is calculated from heat capacities, constituted of two terms: an ideal gas contribution, calculated in this work with the Passut and Danner model [39], and a residual contribution, determined from the SAFT equation of state. For pure hydrogen and methane, the figures S.1, S.2 and S.3 in the Supporting Information show the densities, compressibility factors and Joule-Thomson coefficients, respectively, obtained from the NIST reference database [40] and calculated by our model.

For pure hydrogen, the average deviations between reference data and calculated values for densities, compressibility factors and Joule-Thomson coefficients are equal to 2%, 2% and 7%, respectively. For pure methane, they are equal to 1%, 1% and 4%, respectively. These low deviations validate the pure component parameter selection.

2.2.2 Water and Na^+ and Cl^- ions

The pure water e-PPC-SAFT parameters are taken from the work of Ahmed *et al.* [41], and are recalled in Table 2. More specifically, these parameters have been fitted to accurately reproduce the vapor pressure of pure water, an important property in the context of gas storage in brines to evaluate the quantity of water in the vapor phase.

In order to accurately reproduce the thermodynamic properties of aqueous NaCl solutions for this application, we propose in this work a specific parameterization of the ions Na^+ and Cl^- in a wide range of temperatures (from 0 to 200 °C) and of salt concentrations (from pure water to halite saturation, close to 6 mol/kg_{H2O} at 25 °C). A total of 368 experimental data covering this temperature and salinity ranges were used, including 205 mean ionic activity coefficients [42,43], 87 vapor pressures [44,45] and 76 molar volumes [46]. The parameters of Na^+ and Cl^- are adjusted to match the experimental data using the following objective function:

$$OF = \frac{1}{N}\sum_{i=1}^{N}\left(\frac{\left|X_i^{calc} - X_i^{\exp}\right|}{X_i^{\exp}}\right)^2 \qquad (12)$$

Where *N* is the total number of experimental data.

To reduce the number of adjusted parameters, the following assumptions, originally proposed by Ahmed *et al.* [24], are made. The hard sphere diameters of ions are taken equal to the Pauling diameters, and they are made of only one segment ($m_{ions} = 1$). Ions are assumed to have no dispersive energy ($\varepsilon_{ions} = 0$) but are considered as associative molecules. The number of association sites is taken equal to 7 for Na^+ and 6 for Cl^-. The association volume parameter is arbitrarily taken equal to the one of pure water. Finally, the remaining parameters are considered adjustable: the association energy parameter ε^{AB} of Na^+ and Cl^-, the proportionality factor λ^{MSA} and λ^{Born} (equations (5) and (6)) for the MSA and Born diameters, and the parameters α_0 and α_1 in the dielectric constant model (equation (9)). In the end, a total of 6 adjustable parameters are optimized to fit the 368 experimental data (Table 2).

Table 2. Pure component parameter values for the e-PPC-SAFT equation of state. In bold: parameters optimized in this work.

Parameters	**Water [41]**	**Hydrogen [37]**	**Methane [38]**	**Na+ (this work)**	**Cl- (this work)**
Segment number m (-)	1.02122	1.112	1.03335	1	1
Segment diameter σ^{HS} (Å)	see note	2.906	3.658	1.900	3.620
Dispersion energy ε (K)	207.747	26.627	147.418	-	-
Association energy ε^{AB} (K)	1813.0	-	-	**5569.7228**	**877.8375**
Association volume k^{AB} (-)	0.044394	-	-	0.044394	0.044394
Association sites number (-)	4	-	-	7	6
Dipole Moment μ (D)	1.85	-	-	-	-
Dipole fraction x_p (-)	0.276	-	-	-	-
Diameter factor for MSA λ^{MSA} (-)	-	-	-	**2.1221**	
Diameter factor for Born λ^{Born} (-)	-	-	-	**1.2256**	

Salt effect on dielectric constant α_0 (-)	-	-	-	**-0.0362**
Salt effect on dielectric constant α_1 (K^{-1})	-	-	-	**7.5195**

Note: the segment diameter of pure water is given by:

$$\sigma^{HS} = 2.2423 + 0.51212\exp(0.001126 \cdot T) + 9904.13 / T^2$$

Figure 1 presents the experimental and calculated mean ionic activity coefficient (MIAC) in function of NaCl molality and temperature.

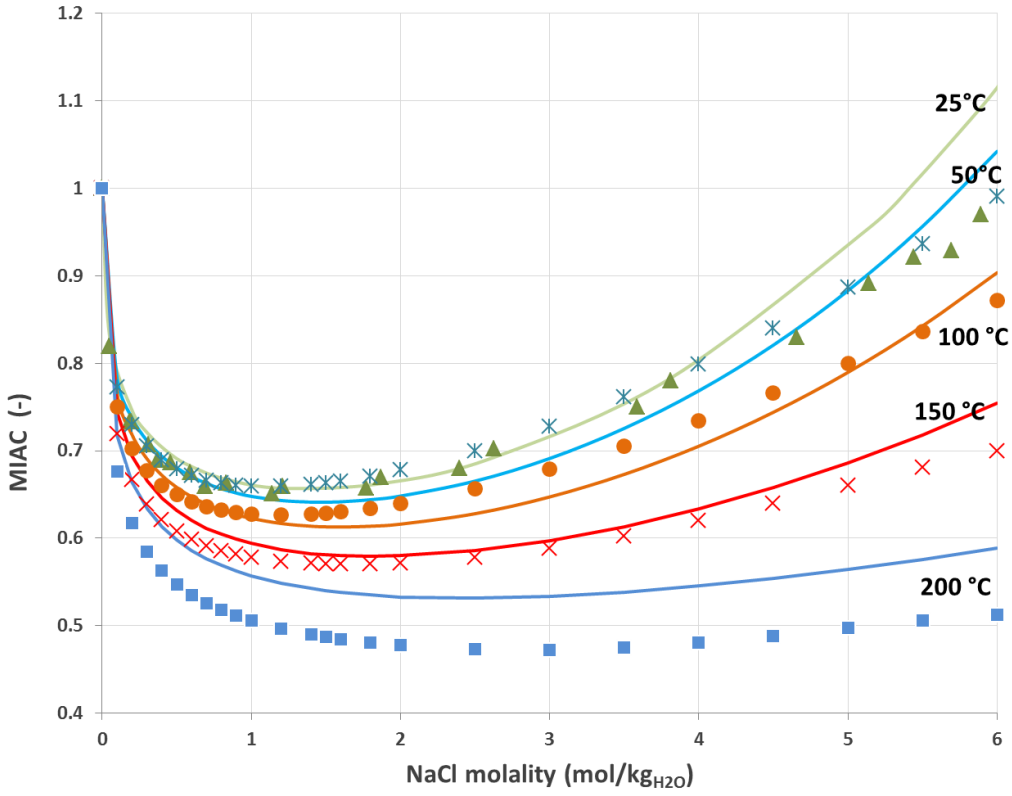

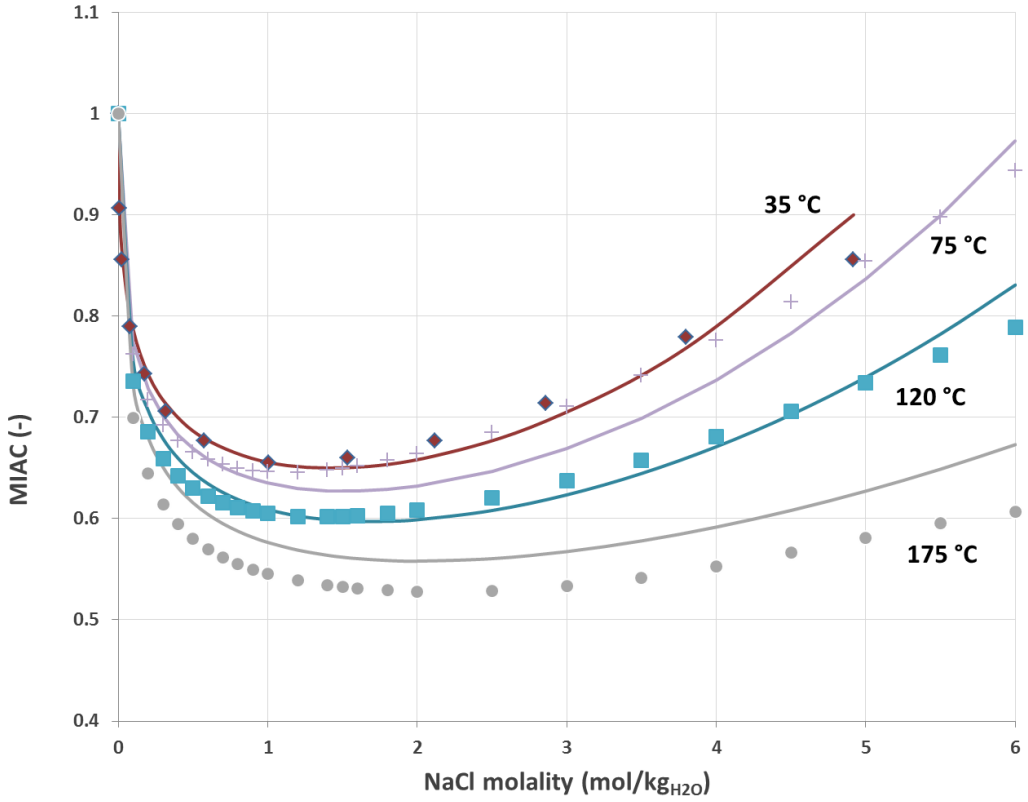

Figure 1. NaCl mean ionic activity coefficient (MIAC). Symbols: experimental data [42,43]. Solid lines: this model.

The MIAC results show a fairly good agreement with the experimental data for the aqueous solution of NaCl at various temperatures and on the whole range of salt concentrations. The overall average deviation is 4.7%. The highest deviations are observed at high temperature (typically above 180 °C) for which the model overestimates the experimental data up to 10%.

Figure 2 compares the model results for saturation pressures with the experimental data. The average deviation (calculated on all experimental points) is 2.3% with a maximal value of 5.8%. The expected trend is well reproduced: the saturation pressure decreases when salt concentration increases. Indeed, when the salt concentration increases, the number of ions to be solvated by water molecules is larger, and consequently water tends to stay in liquid phase rather than to evaporate.

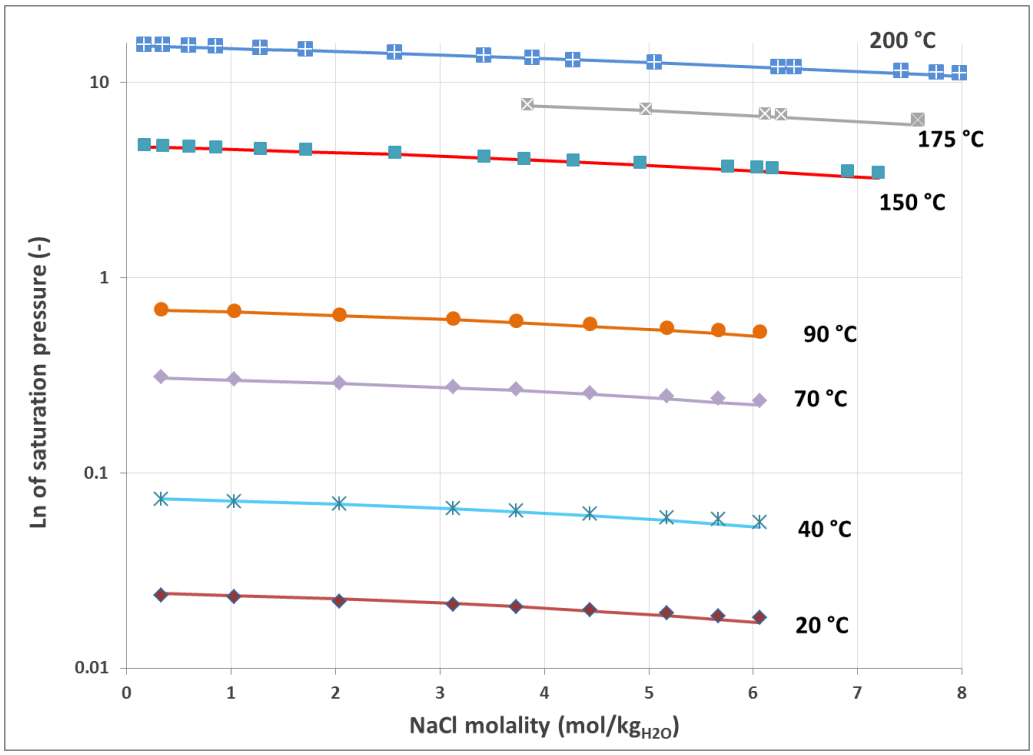

Figure 2. Saturation pressures of aqueous NaCl solution. Symbols: experimental data [44,45]. Solid lines: this model.

Finally, Figure 3 shows experimental data and model results for liquid molar volumes. The average deviation is equal to 0.6% with a maximum value of 1.4%. Here again, the expected trend is well predicted with a diminution of the molar volume when salt concentration increases.

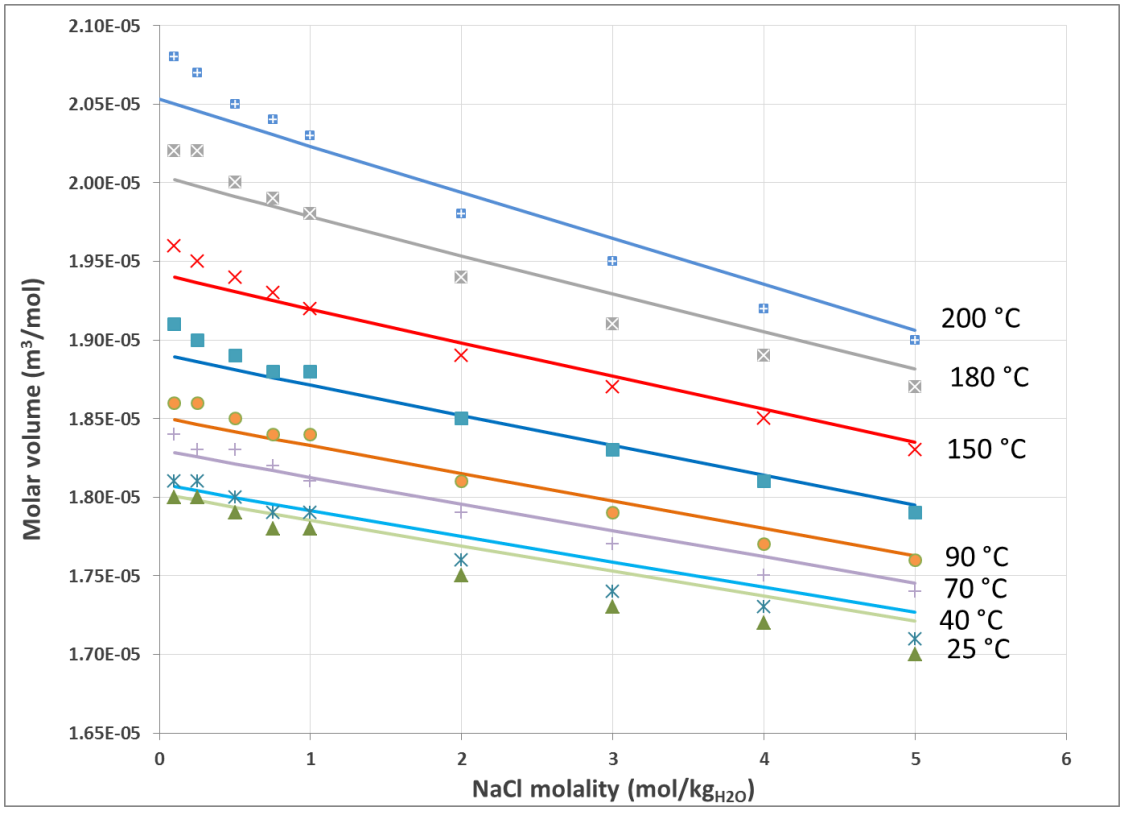

Figure 3. Liquid molar volumes of aqueous NaCl solutions. Symbols: experimental data [46]. Solid lines: this model.

2.3 Mixture parameters: hydrogen and methane in brines

2.3.1 Experimental data

The parameterization of the binary interaction parameters of the e-PPC-SAFT model for the system H_2 + CH_4 + H_2O + Na^+ + Cl^- is carried out on the basis of experimental Henry constants of hydrogen and methane in pure water and in salted water. Concerning hydrogen in pure water, a compilation of more than 250 experimental Henry constants has been done by Lopez-Lazaro *et al.*, who proposed the following empirical correlation fitting these data [26]:

$$T_r \ln\left(\frac{H_i}{P_s^\sigma(T)}\right) = 0.22726 + 9.1114\left(1-T_r\right)^{0.355} - 1.38821\cdot T_r\left(\frac{1}{T_r}-1\right)^{1.5} \qquad (13)$$

where T_r is the reduced temperature of water ($T_r = T/T_c$ with T in Kelvin and T_c = 647.096 K), and $P_s^\sigma(T)$ the vapor pressure (in Pa) of pure water at temperature T. The hydrogen Henry constants generated with this correlation will be further denoted as "correlated data" and are plotted on Figure 4.

For methane in pure water, Harvey [47] proposed an empirical correlation fitting the available experimental data:

$$\ln H_i = \ln P_s^\sigma + \frac{-11.0094}{T_r} + \frac{4.8362}{T_r}\left(1-T_r\right)^{0.355} + 12.522\exp\left(1-T_r\right)\left(T_r\right)^{-0.41} \qquad (14)$$

where Henry constant and saturation pressure are expressed here in MPa. As for hydrogen, the methane Henry constants generated with this correlation will be further denoted as "correlated data" and are plotted on Figure 4.

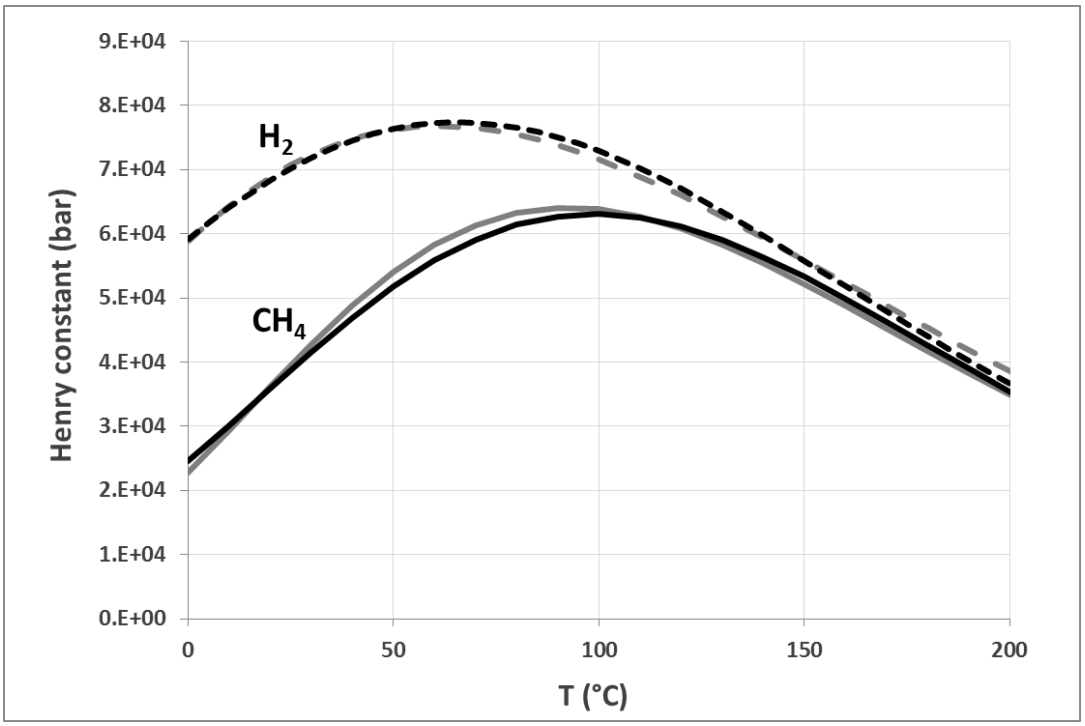

Figure 4. Henry constants of hydrogen (dotted lines) and methane (solid lines). Black: this model. Gray: correlated data (equation (13), equation (14)).

Concerning Henry constants of hydrogen in salted water, experimental data are very scarce and restricted to low temperatures (up to 30 °C) and moderate salinities (2 mol_{NaCl}/kg_{H2O}). Lopez-Lazaro *et al.* proposed a critical review of these data, and computed new data at higher temperatures using a molecular simulation technique. An uncertainty of 10% was evaluated for both experimental and simulation data [26]. Figure 5 shows both experimental and molecular simulation data.

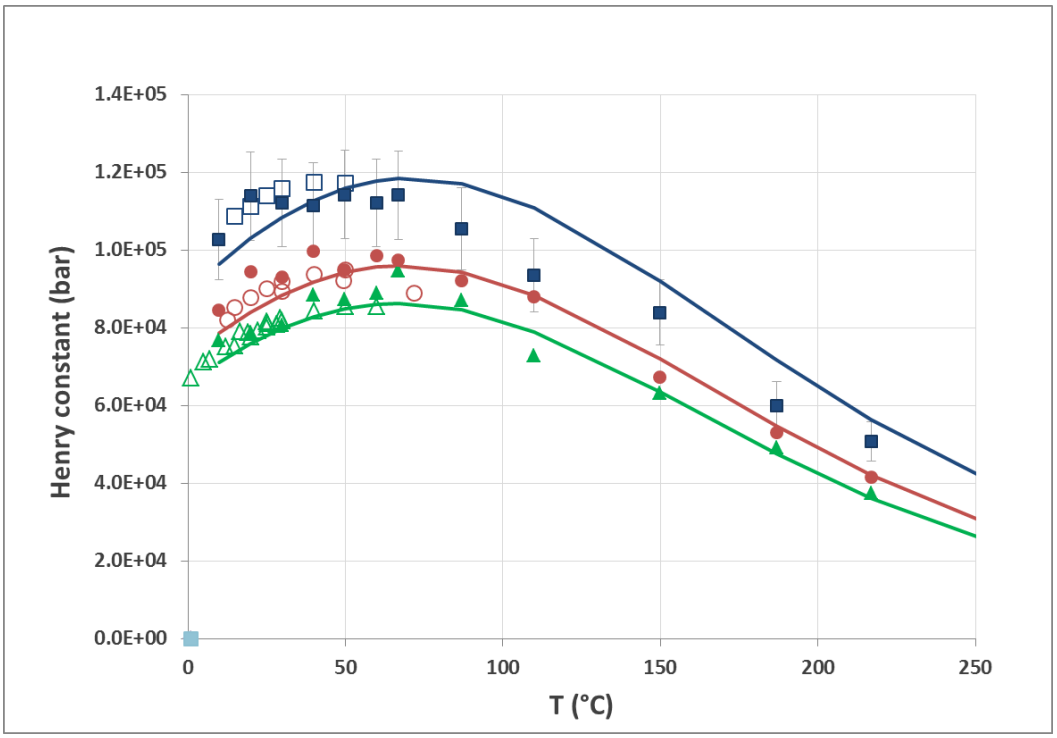

Figure 5. Henry constant of hydrogen in salted water. Open symbols: experimental data [48,49]. Filled symbols: data from molecular simulation [26]. Solid lines: this model. Triangles: m_{NaCl} = 0.5 mol/kg$_{H2O}$. Circles: m_{NaCl} = 1 mol/kg$_{H2O}$. Squares: m_{NaCl} = 2 mol/kg$_{H2O}$.

Concerning methane in salted water, experimental Henry constants have been reported by Cramer *et al.* [50] on a wide temperature range (0 to 300 °C) and for salt molalities up of to 4.3 mol$_{NaCl}$/kg$_{H2O}$. However, the experimental data at the highest salt concentration are very scattered and were therefore not considered for parameter regression. Furthermore, in order to be the most reliable in the temperature range of interest for gas storage in salt caverns, we focused only on experimental data up to 200 °C. The selected data are plotted on Figure 6.

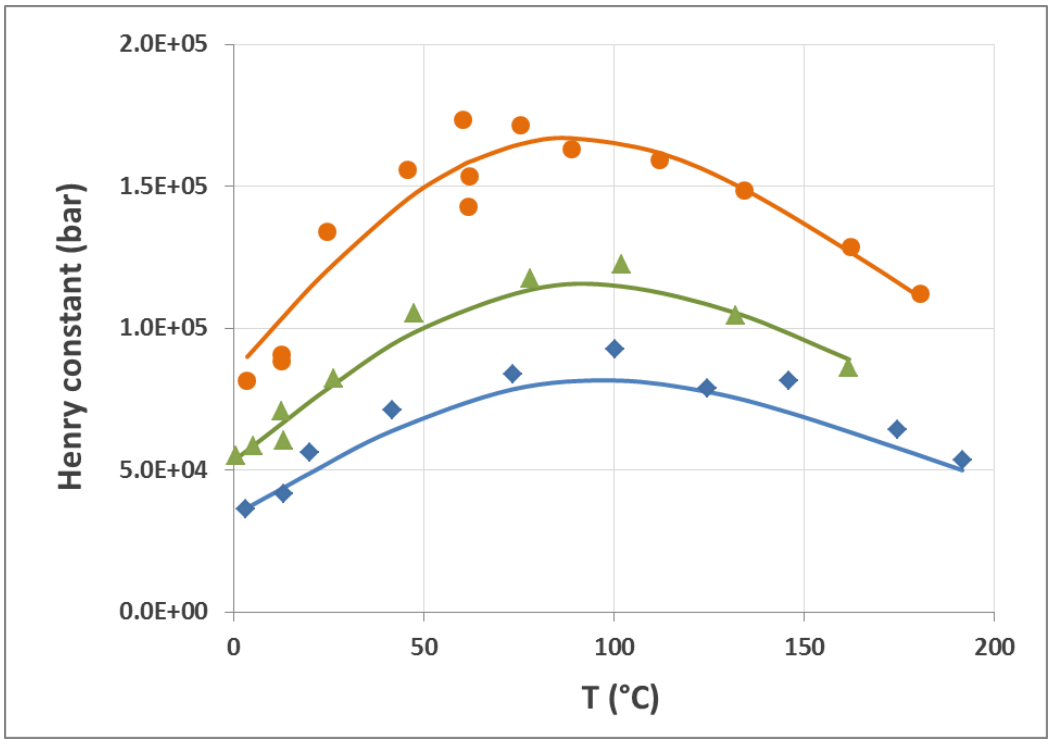

Figure 6. Henry constant of methane in salted water. Symbols: experimental data [50]. Solid lines: this model. Triangles: m_{NaCl} = 0.8 mol/kg$_{H2O}$. Circles: m_{NaCl} = 1.9 mol/kg$_{H2O}$. Squares: m_{NaCl} = 3 mol/kg$_{H2O}$.

2.3.2 Binary interaction parameters fitting

In order to accurately reproduce the experimental Henry constants of both hydrogen and methane in pure and salted water, an adjustment of binary interaction parameters is required. As stated in Table 1, two binary parameters are tunable in the e-PPC-SAFT framework: the k_{ij} parameter (acting on dispersive energy), and the l_{ij} parameter (acting on the cross-diameter of non-additive hard spheres). From theoretical and molecular simulation studies [26,33], Trinh *et al.* and Lopez-Lazaro *et al.* showed that hydrogen solubility is considerably more influenced by the l_{ij} parameter rather than the k_{ij} parameter. Thus, it was decided in this work to set all k_{ij} binary parameter to 0 and adjust only l_{ij} binary parameters, for hydrogen and for methane. To increase accuracy at elevated temperatures, a temperature-dependence is introduced in this binary parameter:

$$l_{ij}(T) = l_{ij}^{(2)} \cdot T^2 + l_{ij}^{(1)} \cdot T + l_{ij}^{(0)} \qquad (15)$$

The l_{ij} parameter between H_2 and water is adjusted to match the correlated experimental data generated by equation (13). The optimized parameters are given in Table 3, and a comparison between data and model is provided on Figure 4. The average deviation is about 1.4% for the considered range of temperatures (from 0 to 200 °C). The l_{ij} parameter between methane and water is adjusted on correlated data given by equation (14), and Figure 4 shows a comparison between correlated data and the model. The average deviation is about 2.5% on the same temperature range.

For hydrogen solubility in salted water, a unique binary interaction parameter l_{ij} between H_2 and ions Na^+ and Cl^- is adjusted to match the experimental data. It is found that a constant value (reported in Table 3) is sufficient enough to obtain a good accuracy. A comparison between experimental and modeling results is provided on Figure 5. The average deviation is equal to 4.7%, which is less than

the estimated experimental uncertainties. For Henry constant of methane in salted water, a temperature dependence is needed for the l_{ij} parameter between methane and ions. The optimized parameters are provided in Table 3, and the average deviation is equal to 7%. The Figure 6 provides a comparison between experimental data and model results.

Table 3. Binary interaction parameters optimized for the system H_2+CH_4+H_2O+Na^++Cl^-

Binary parameter	$l_{ij}^{(2)}$ (K^{-2})	$l_{ij}^{(1)}$ (K^{-1})	$l_{ij}^{(0)}$ (-)
H_2-H_2O	$7.5537 \cdot 10^{-7}$	$-5.8906 \cdot 10^{-4}$	0.14367
H_2-Na^+ H_2-Cl^-	-	-	-0.06395
CH_4-H_2O	$7.7229 \cdot 10^{-7}$	$-6.5424 \cdot 10^{-4}$	0.13797
CH_4-Na^+ CH_4-Cl^-	-	$4.9682 \cdot 10^{-4}$	-0.25152

2.4 Model predictions and validation

Although parameterized only on Henry constant data (or, in other words, on solubility data in liquid phase), this thermodynamic model is also able to accurately predict the composition of the vapor phase, what is of primary importance in the context of gas storage to evaluate the moisture content of the gas produced during withdrawal. Figure 7 and Figure 8 present an example of pressure-composition diagram of H_2 + H_2O and CH_4 + H_2O systems, respectively, in typical operating conditions of gas storage, showing a very good agreement in both liquid and vapor phase compositions. Unfortunately, there is no experimental data available in open literature on the vapor phase composition in salted water to extend this comparison. It can also be noticed that the Henry law validity domain is very large for hydrogen in water, typically up to 600 bar if we refers to high-pressure experimental data of Wiebe *et al.* [51]. For methane, Figure 8 also shows that the liquid phase composition is correctly predicted even at high pressure where the Henry law is no longer valid. More specifically, the mutual solubilities of methane in water is well predicted up to 300 bar. Thus, the model developed in this work covers well the operating conditions met in gas storage applications.

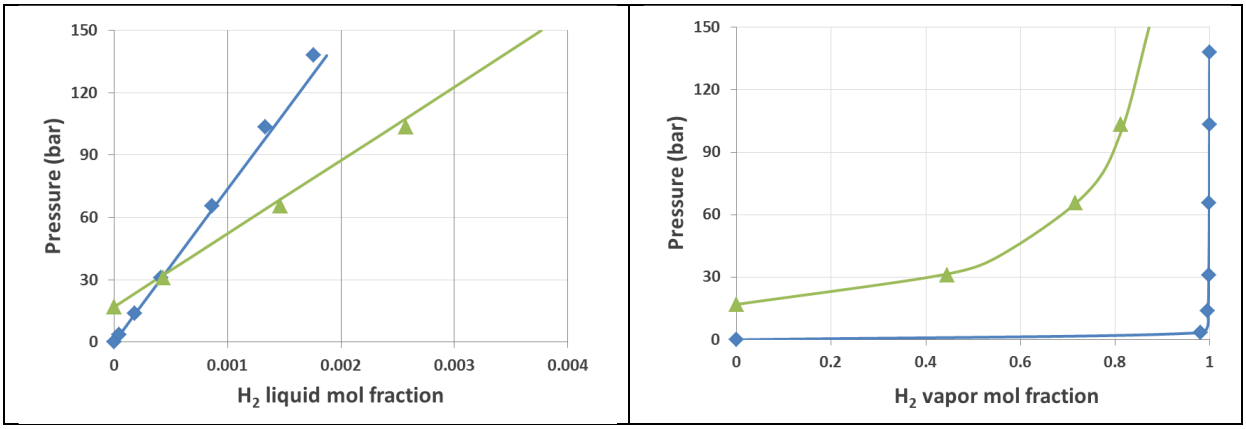

Figure 7. Pressure-composition diagram of the H_2+H_2O system (left: bubble curves; right: dew curves). Symbols: experimental data [52]. Solid lines: this model. Diamonds: 37.8 °C. Triangles: 204.5 °C.

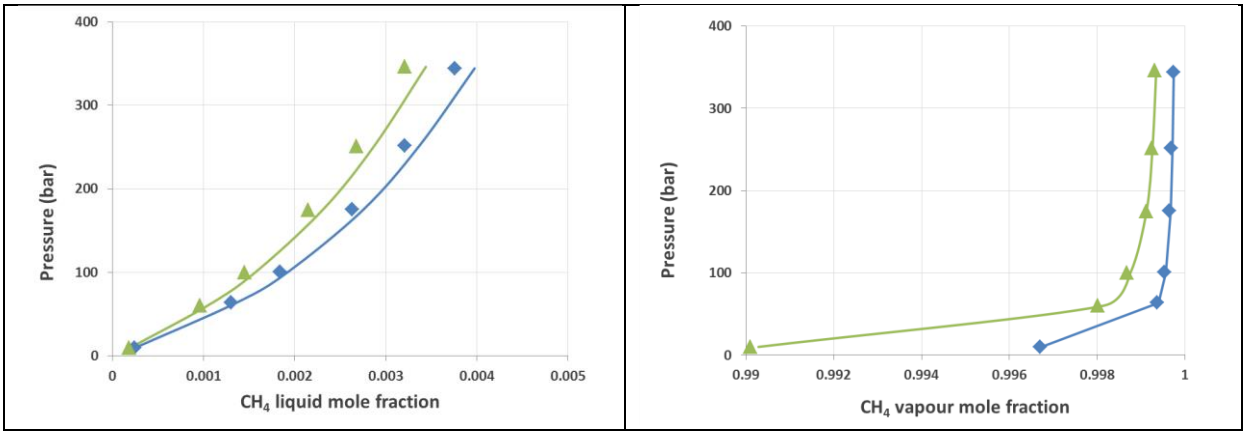

Figure 8. Pressure-composition diagram of the CH_4+H_2O system (left: bubble curves; right: dew curves). Symbols: experimental data [53]. Solid lines: this model. Diamonds: 25 °C. Triangles: 40 °C.

The model predictions can also be compared to results provided by the solubility model recently developed by Li *et al.* [27]. Contrarily to our modeling work in which an homogeneous approach is adopted (the same thermodynamic model is used for both liquid and vapor phases), Li *et al.* proposed an heterogeneous approach, using Henry constants, Poynting corrections and an activity coefficient model (Pitzer) for the aqueous phase, and a pure-hydrogen equation of state for the vapor phase. The Figure S.4 in the Supporting Information presents a comparison of both models on hydrogen solubility at low pressure (1 bar) and high pressure (300 bar), for salinities of 0, 2 and 4 mol_{NaCl}/kg_{H2O}, and for temperatures ranging from 0 to 100 °C (validity range of the Li *et al.* model).

Results of both models are found in good agreement. The average deviations between models are equal to 8% at 1 bar, and 14% at 300 bar, which is also the order of magnitude of experimental uncertainties for salted systems data. It can be noticed that the Li *et al.* model estimates vapor phase composition following an ideal gas behavior assumption. This can explain why deviations are larger at high pressure. Our modeling approach is based on a real flash calculation to calculate compositions, and involves an equation of state for the mixture in the vapor phase. Thus, better predictions are expected at high pressure with our model.

3 Case-study: application to gas storage in salt caverns

In this section, the e-PPC-SAFT equation of state is applied to a case-study of gas storage in salt caverns. The performance of an existing methane storage is compared to that of two *fictitious* storages of, respectively, hydrogen, and a mixture composed of 80 vol.% methane and 20 vol.% hydrogen.

3.1 Model description

A numerical model of salt cavern storage [31] is used to describe gas flow in the well (from the well-head to the well shoe) and the cavern (represented as a one-dimension spherical gas tank embedded in a finite rock mass), and to estimate evolutions of temperature and pressure during gas injection and withdrawal. The mathematical system solved is a coupled nonlinear thermo-hydraulic problem that accounts for heat exchanges with the rock mass.

Usually, a first phase consists in optimizing the numerical model to reproduce the available monitored field data: pressure and temperature at the wellhead. The main calibration parameters of this history-matching step are the shape factor of the cavern, which impacts heat exchanges with the rock mass, and its volume. Once optimized, the model can be used to plan future gas storage operations in this cavern.

In the present case-study, the properties of the cavern are those of an existing methane cavern storage, and are summarized in Table 4. The cavern volume is 570 000 m^3; it has been considered constant during the whole simulation: salt creeping is neglected, as the simulated time period is short. The residual volume of brine that remains in the cavern after debrining was estimated at 5000 m^3. The minimum and maximum admissible pressures at the casing shoe (which corresponds to the top of the cavern) are driven by geology and stability of the cavern, and were respectively equal to 60 and 240 bar. Finally, the rock mass temperature at cavern depth has been determined equal to 53 °C.

Table 4: Case-study model parameters

Characteristics	**Value**
Cavern depth (m)	1 300
Cavern volume (m^3)	570 000
Minimum admissible cavern pressure (bar)	60
Maximum admissible cavern pressure (bar)	240
Rock mass temperature at cavern depth (°C)	53

Rock salt is considered as pure halite (NaCl). Salinity in the brine is calculated considering the halite solubility as a function of temperature from [54].

The gas is considered completely dry at injection and initially at a temperature of 30 °C. In the cavern, thermodynamic equilibrium is assumed to occur instantaneously. This hypothesis induces an overestimation of the water content in the gas. Indeed, in real storages, gas is not always fully saturated with vapor. Natural convection stirs gas and vapor in the upper part of the cavern and favors mixing. However, gas temperature may be lower at the bottom of the cavern because sump brine is colder than the gas phase. This hinders natural convection near the brine-gas interface and prevents

thermodynamic equilibrium [11,13]. Nonetheless, this upper-bound evaluation provides an useful constraint to design and operate surface facilities [12].

3.2 Salt cavern model simulation results for methane, hydrogen and the mixture

The simulated storage scenario is a first 6-months-long (180 days) withdrawal phase, starting from the maximum admissible pressure down to the minimum one, followed by a 6-months-long injection step to reach the maximum pressure again. Two of these cycles were modeled, for a total simulated period close to two years (720 days).

From these constraints, the numerical model determined, for each of the considered gases (pure methane, pure hydrogen and mix), the constant flow rate of withdrawal (or injection), the working and cushion gas volumes (gas volume which can be withdrawn from a storage cavern and gas volume necessary to ensure the minimum storage pressure, respectively), the pressure variations at the well head and the temperature variations in the cavern (pressure in the cavern varies between the minimum and maximum cavern admissible pressure). These results are reported in Table 5, and plotted on figure S.5 and S.6 in the Supporting Information.

Table 5: Calculated flow rates and working gas volume and mass for methane, hydrogen and mixture storages

	Methane	**Hydrogen**	**Mix**
Mass flow (t/day)	374.9	33.3	255.5
Volumetric flow (Nm^3/day)	475 000	370 000	432 000
Working gas volume (Nm^3)	86.7×10^6	70.6×10^6	78.8×10^6
Working gas mass (t)	68 430	6 350	46 600
Cushion gas volume (Nm^3)	32.0×10^6	31.2×10^6	31.7×10^6
Cushion gas mass (t)	20 991	2 810	18 772

As shown in Figure S.5 in the Supporting Information, well head pressure for hydrogen is almost equal to the cavern pressure (that varies between 60 and 240 bar). The difference between wellhead pressure and cavern pressure is about 0.5 to 2 bar for hydrogen and about 5 to 20 bar for methane. Hydrogen is less dense than methane. Moreover, the higher the dynamic viscosity, the higher are pressure losses by friction in the well. For example at 1 °C and 150 bar, pure hydrogen dynamic viscosity is almost 9 µPa.s, while methane viscosity is 17 µPa.s for natural gas [55].

Lower viscosity and weight well column (i.e lower gas density) for hydrogen compared to methane explains why well head and cavern pressures remain close in hydrogen simulations. Behavior of the mix is very similar to the methane one.

The Figure S.6. in the Supporting Information shows that the amplitude of temperature changes during one cycle is less for hydrogen compared to methane. Hydrogen does not cool down as much as natural gas: in the first six months, the temperature drop for hydrogen is about 25 °C, while it is

32 °C for natural gas and 29 °C for the mix. As the Joule Thomson coefficient of hydrogen is negative (see Figure S.3 in the Supporting Information), hydrogen should warm up slightly if the expansion is isenthalpic. However, heat exchanges with surrounding rock salt induce enthalpy changes: hydrogen temperature still increases during injection and decreases during withdrawal. That can explain why temperature variations for hydrogen are smaller than for natural gas or mix.

Finally, it is important to point out that, for the same pressure and volume of gas in the cavern, there is more mass of natural gas than hydrogen, as the density of hydrogen is approximately 8 times smaller than the natural gas one (at normal conditions, 0.0899 kg/m^3 for hydrogen against 0.7893 kg/m^3 for natural gas). Hydrogen is 2.5 more energetic by quantity of mass than natural gas (in term of High Heating Value). But when compared in energy per volume, natural gas is about 3 times more energetic than hydrogen. Thus, less energy is stored in a cavern filled with hydrogen rather than with methane or mix.

3.3 Gas-brine phase equilibrium simulation results

The e-PPC-SAFT EoS makes it possible to evaluate the water content in the gaseous phase and the amount of gas dissolved in the aqueous phase for each one of the three gases considered during storage cycles. These simulations were performed considering an halite-saturated brine, and compared with pure water (Figure 9, Figure 10, Figure 11).

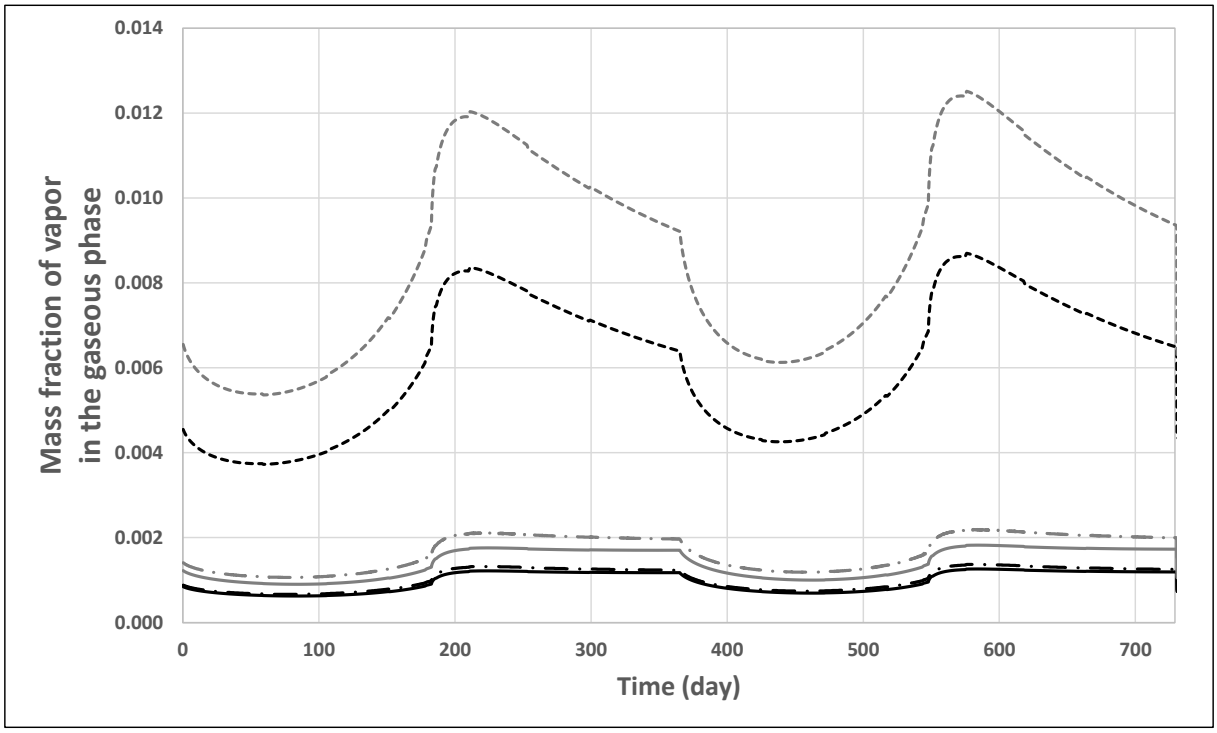

Figure 9: Vapor mass fraction in the gaseous phase during the withdrawal-injection cycles for methane (solid line), hydrogen (dotted line) and mix between hydrogen and methane (dot-dashed line) storages considering brine (black color) or pure water (grey color) as the residual fluid after debrining.

Whatever the kind of stored gas, the mass fraction of water in the gas phase is less when gas is in equilibrium with brine compared to pure water (Figure 9). This has to be related to the polar nature of the water: in brine, ions are solvated by water molecules that makes the water evaporation more difficult, as more energy is needed to overcome solvation forces.

The e-PPC-SAFT model estimates a maximum water mass fraction in gas phase during the cycle, that can be used to size surface facilities. Mass fraction of water in the hydrogen gas phase is about 5 times more compared to the methane gas phase (Figure 9), while behavior of the mix remains close to the pure methane one.

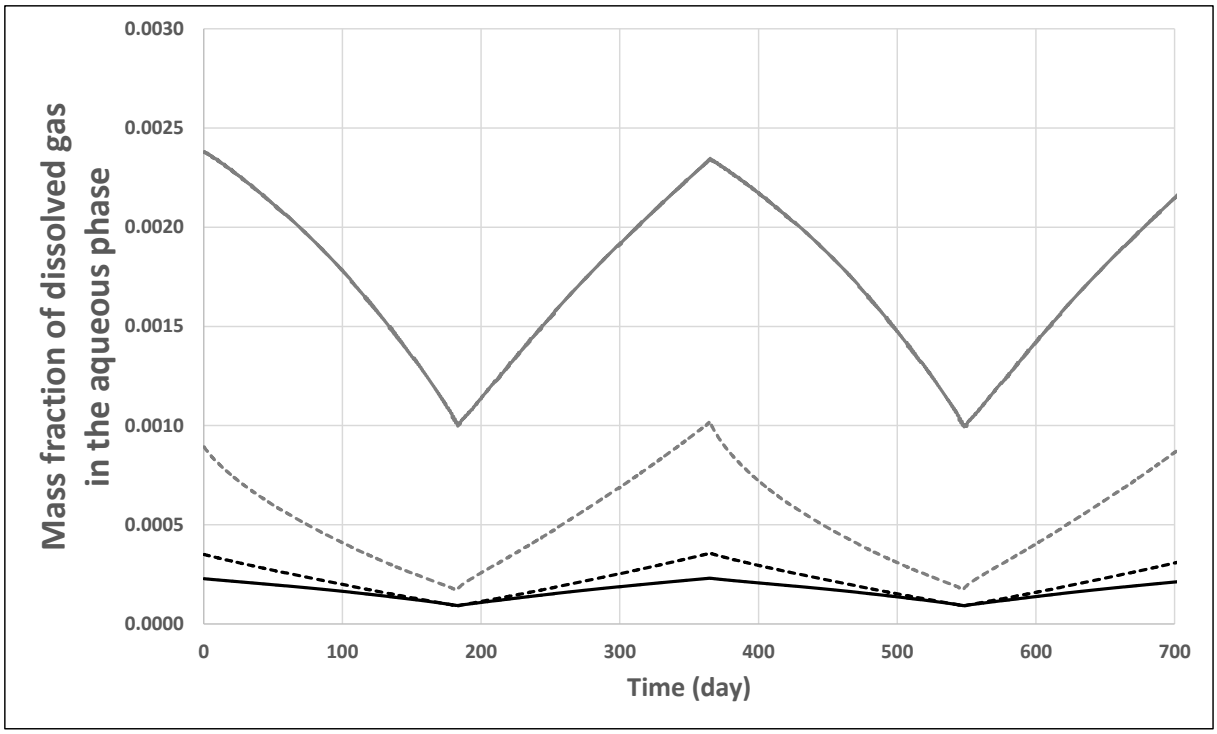

Figure 10: Mass fraction of dissolved methane in the liquid phase for methane storage (solid line) and dissolved hydrogen for hydrogen storage (dotted line) considering brine (black color) or pure water (grey color) as the residual fluid after debrining.

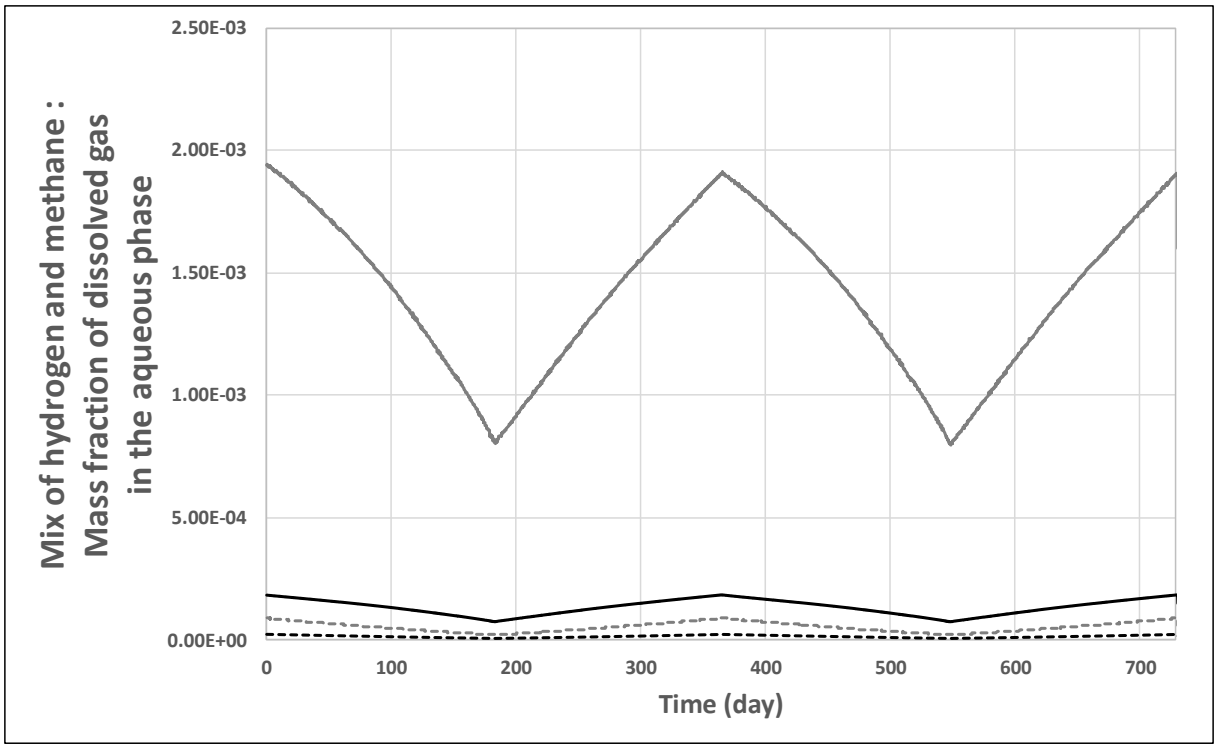

Figure 11: Mass fraction of dissolved methane (solid line) and dissolved hydrogen (dotted line) in the liquid phase for a mix storage considering brine (black color) or pure water (grey color) as the residual fluid after debrining.

The amount of gas lost by dissolution in pure water or brine may be estimated at the minimum of the pressure and temperature conditions met during the cycle (Figure 10 and Figure 11). It also corresponds to the lowest amount of gas dissolved in the aqueous phase. Gas lost in brine is actually much lower than in pure water due to the "salting-out" effect. For the cavern defined above with an estimate of 5000 m^3 of brine or water remaining in the cavern after debrining, the maximum mass of H_2 lost by dissolution would be about 2 tons in brine versus 5 tons in pure water. It is slightly less than for methane or mix for the same cavern. In practice, this value represents an upper limit as equilibrium may never be reached.

4 Conclusions

In this work, the e-PPC-SAFT equation of state has been parameterized to predict phase equilibrium of systems H_2 + CH_4 + H_2O + Na^+Cl^- for conditions of temperature, pressure and salinities of interest for the gas storage application in salt caverns. The ions parameters have been adjusted by focusing specifically on the association and electrostatic terms of the equation of state, and to match salted water properties: this thermodynamic model is then able to reproduce with a good accuracy the properties of NaCl aqueous solutions such as mean ionic coefficient activities, vapor pressures and molar densities. Furthermore, binary interaction parameters between hydrogen (or methane) and water, Na^+ and Cl^- have been adjusted to match gas solubility data. As a consequence, this model is able to predict correctly phase compositions of the systems H_2 + H_2O + NaCl and CH_4 + H_2O + NaCl. The validity ranges of this model are 0 to 200 °C for temperatures, 0 to 300 bar for pressures, and 0 to 8 mol_{NaCl}/kg for salinities. Results are found to be comparable with an existing model for H_2 + CH_4 + H_2O + Na^+Cl^- [27], but probably more accurate in extrapolation due to the rigorous physics behind the e-PPC-SAFT framework.

The e-PPC-SAFT model has been used to model gas injection / withdrawn in salt caverns. The performance of an existing methane storage in a cavern has been compared to that of two hypothetical storages of, respectively, hydrogen, and a mixture composed of 80 vol.% methane and 20 vol.% hydrogen. From a thermodynamic point of view, integrating up to 20% of hydrogen in caverns does not have a major influence on temperature, pressure and water content compared to pure methane storage. A pure hydrogen storage exhibits a slightly different behavior than pure methane: wellhead pressure is closer to the cavern pressure, and the amplitude of temperature changes is lower.

With this new thermodynamic model, the simulation carried out may be used for storage designs and operations. It should be noticed that such a study assumes that thermodynamic equilibrium is instantaneously reached in the cavern. The future work will quantify precisely deviations from thermodynamic equilibrium using Computational Fluid dynamics approach describing fluid flows and heat and mass exchanges in the cavern.

5 References

[1] International Energy Agency. The Future of Hydrogen - Seizing today's opportunities. Report prepared by the IEA for the G20, Japan 2019, 2019.

[2] Ghryd Project. http://grhyd.fr.

[3] HyDeploy Project. http://hydeploy.co.uk.

[4] Panfilov M. Underground and pipeline hydrogen storage. In: Subramani, Basile et al. (Ed.) 2015 – Compendium of hydrogen energy, p. 91–115.

[5] Underground Sun Storage. https://www.underground-sun-storage.at/en.html.

[6] Pérez AC, Pérez EV, Bolcich JC. Patagonia Wind - Hydrogen Project: Underground Storage and Methanation. 21st World Energy Conference 2016. Zaragoza, Spain. 13-16th June, 2016.

[7] INERIS. Transition Energétique - Stockage souterrain de l'hydrogène. Rapport INERIS DRS-15-10182-03229B.

[8] Ozarslan A. Large-scale hydrogen energy storage in salt caverns. International Journal of Hydrogen Energy 2012;37(19):14265–77. https://doi.org/10.1016/j.ijhydene.2012.07.111.

[9] Tarkowski R. Underground hydrogen storage: Characteristics and prospects. Renewable and Sustainable Energy Reviews 2019;105:86–94. https://doi.org/10.1016/j.rser.2019.01.051.

[10] Crotogino F. Chapter 20 - Larger Scale Hydrogen Storage. In: Letcher TM, editor. Storing Energy. Oxford: Elsevier; 2016, p. 411–429.

[11] Bérest P. Heat transfer in salt caverns. International Journal of Rock Mechanics and Mining Sciences 2019;120:82–95. https://doi.org/10.1016/j.ijrmms.2019.06.009.

[12] Louvet F, Charnavel Y, Portenabe JC. Moisture content of Gas in Salt Caverns Surface Measurements. SMRI Fall Meeting 2018, 2018.

[13] Berest P, Louvet F. Aspects of the Thermodynamic Behavior of Salt Caverns. SMRI Fall Meeting 2019, 2019.

[14] Duan ZH, Moller N, Greenberg J, Weare JH. The Prediction of Methane Solubility in Natural-Waters to High Ionic-Strength from O-Degrees-C to 250-Degrees-C and from 0 to 1600 Bar. Geochim.Cosmochim.Acta 1992;56(4):1451–60.

[15] Duan ZH, Sun R. An improved model calculating CO2 solubility in pure water and aqueous NaCl solutions from 273 to 533 K and from 0 to 2000 bar. Chem.Geol. 2003;193(3-4):257–71.

[16] Duan ZH, Mao SD. A thermodynamic model for calculating methane solubility, density and gas phase composition of methane-bearing aqueous fluids from 273 to 523 K and from 1 to 2000 bar. Geochim.Cosmochim.Acta 2006;70(13):3369–86.

[17] Zuo YX, Guo TM. Extension of the Patel-Teja equation of state to the prediction of the solubility of natural gas in formation water. Chem.Eng.Sci. 1991;46(12):3251–8.

[18] Soreide I, Whitson C. Peng-Robinson predictions for hydrocarbons, CO_2, N_2, and H_2S with pure water and NaCl brine. Fluid Phase Equilib. 1992;77:217–40.

[19] Sorensen H, Pedersen KS, Christensen PL. Modeling of gas solubility in brines. Org.Geochem. 2002;33:635–42.

[20] Patel BH, Paricaud P, Galindo A, Maitland GC. Prediction of the Salting-Out Effect of Strong Electrolytes on Water + Alkane Solutions: Industrial & Engineering Chemistry Research. Ind.Eng.Chem.Res. 2003;42(16):3809–23. https://doi.org/10.1021/ie020918u.

[21] Duan Z, Moller N, Weare JH. Equations of State for the NaCl-H_2O-CH_4 System and the NaCl-H_2O-CO_2-CH_4 System: Phase Equilibria and Volumetric Properties above 573 K. Geochim.Cosmochim.Acta 2003;67:671–80.

[22] Li J, Wei L, Li X. An improved cubic model for the mutual solubilities of CO2–CH4–H2S–brine systems to high temperature, pressure and salinity. Applied Geochemistry 2015;54:1–12. https://doi.org/10.1016/j.apgeochem.2014.12.015.
[23] Courtial X, Ferrando N, Hemptinne J-C de, Mougin P. Electrolyte CPA equation of state for very high temperature and pressure reservoir and basin applications. Geochim.Cosmochim.Acta 2014;142:1–14. https://doi.org/10.1016/j.gca.2014.07.028.
[24] Ahmed S, Ferrando N, Hemptinne J-C de, Simonin J-P, Bernard O, Baudouin O. Modeling of mixed-solvent electrolyte systems. Fluid Phase Equilib. 2018;459:138–57. https://doi.org/10.1016/j.fluid.2017.12.002.
[25] Rozmus J, Hemptinne JC de, Galindo A, Dufal S, Mougin P. Modeling of Strong Electrolytes with ePPC-SAFT up to High Temperatures: Industrial & Engineering Chemistry Research. Ind.Eng.Chem.Res. 2013;52:9979–94. https://doi.org/10.1021/ie303527j.
[26] Lopez-Lazaro C, Bachaud P, Moretti I, Ferrando N. Predicting the phase behavior of hydrogen in NaCl brines by molecular simulation for geological applications. BSGF - Earth Sci. Bull. 2019;190. https://doi.org/10.1051/bsgf/2019008.
[27] Li D, Beyer C, Bauer S. A unified phase equilibrium model for hydrogen solubility and solution density. International Journal of Hydrogen Energy 2018;43(1):512–29. https://doi.org/10.1016/j.ijhydene.2017.07.228.
[28] Chabab S, Théveneau P, Coquelet C, Corvisier J, Paricaud P. Measurements and predictive models of high-pressure H2 solubility in brine (H2O+NaCl) for underground hydrogen storage application. International Journal of Hydrogen Energy 2020. https://doi.org/10.1016/j.ijhydene.2020.08.192.
[29] Bazarkina EF, Chou I-M, Goncharov AF, Akinfiev NN. The Behavior of H2 in Aqueous Fluids under High Temperature and Pressure. Elements 2020;16(1):33–8. https://doi.org/10.2138/gselements.16.1.33.
[30] Gross J, Sadowski G. Perturbed-Chain SAFT: An equation of state based on a perturbation theory for chain molecules. Ind.Eng.Chem.Res. 2001;40:1244–60.
[31] Masson R, Jeannin L, Louvet F, Vuddamalay A. Domain decomposition methods to model heat exchanges between a well and a rock mass. Computational Geosciences 2020;24(3):1377–92. https://doi.org/10.1007/s10596-020-09957-2.
[32] Nguyen-Huynh D, Passarello J-P, Tobaly P, Hemptinne J-C de. Application of GC-SAFT EOS to polar systems using a segment approach. Fluid Phase Equilib. 2008;264(1-2):62–75. https://doi.org/10.1016/j.fluid.2007.10.019.
[33] Trinh T-K-H, Passarello J-P, Hemptinne J-C de, Lugo R, Lachet V. A non-additive repulsive contribution in an equation of state: The development for homonuclear square well chains equation of state validated against Monte Carlo simulation. J CHEM PHYS 2016;144(12). https://doi.org/10.1063/1.4944068.
[34] Fawcett WR. Thermodynamic Parameters for the Solvation of Monatomic Ions in Water. J. Phys. Chem. B 1999;103(50):11181–5. https://doi.org/10.1021/jp991802n.
[35] Simonin JP. Real ionic solutions in the mean spherical approximation .2. Pure strong electrolytes up to very high concentrations, and mixtures, in the primitive model. J.Phys.Chem.B 1997;101(21):4313–20.
[36] Schreckenberg JMA, Dufal S, Haslam AJ, Adjiman CS, Jackson G, Galindo A. Modelling of the thermodynamic and solvation properties of electrolyte solutions with the statistical associating fluid theory for potentials of variable range. Mol.Phys. 2014;112(17):2339–64. https://doi.org/10.1080/00268976.2014.910316.

[37] Trinh T-K-H, Passarello J-P, Hemptinne J-C de, Lugo R. Use of a non additive GC-PPC-SAFT equation of state to model hydrogen solubility in oxygenated organic compounds. Fluid Phase Equilib. 2016;429:177–95. https://doi.org/10.1016/j.fluid.2016.08.003.
[38] Nguyen-Huynh D, Hemptinne JC de, Lugo R, Passarello JP, Tobaly P. Modeling Liquid-Liquid and Liquid-Vapor Equilibria of Binary Systems Containing Water with an Alkane, an Aromatic Hydrocarbon, an Alcohol or a Gas (Methane, Ethane, CO2 or H2S), Using Group Contribution Polar Perturbed-Chain Statistical Associating Fluid Theory. Ind.Eng.Chem.Res. 2011;50(12):7467–83. https://doi.org/10.1021/ie102045g.
[39] Passut CA, Danner RP. Correlation of ideal gas enthalpy, heat capacity, and entropy. Ind.Eng.Chem.Proc.Des.Dev. 1972;11(4):543–6.
[40] NIST and TRC database, National Institute of standards and Technology Thermodynamics and Thermodynamics Research Center, version 2-2011-3-Pro; 2011.
[41] Ahmed S, Ferrando N, Hemptinne J-C de, Simonin J-P, Bernard O, Baudouin O. A New PC-SAFT Model for Pure Water, Water–Hydrocarbons, and Water–Oxygenates Systems and Subsequent Modeling of VLE, VLLE, and LLE. J. Chem. Eng. Data 2016;61(12):4178–90. https://doi.org/10.1021/acs.jced.6b00565.
[42] Hernández-Luis F, Rodríguez-Raposo R, Ruiz-Cabrera G. Activity coefficients of NaCl in aqueous mixtures with ε-increasing co-solvent: N-methylformamide–water mixtures at 298.15K. Fluid Phase Equilib. 2011;310(1):182–91. https://doi.org/10.1016/j.fluid.2011.08.018.
[43] Gibbard HF JR., Scatchard G, Rousseau RA, Creek JL. Liquid-Vapor Equilibrium of Aqueous Sodium Chloride, from 298 to 373K and from 1 to 6 mol kg-1, and Related Properties. J.Chem.Eng.Data 1974;19(3):281–8.
[44] Mokbel I, Ye S, Jose J, Xans P. Study of non ideality of various aqueous sodium chloride solutions by vapor pressure measurements and correlation of experimental results by Pitzer's method. J.Chim.Phys.PCB 1997;94:122–37.
[45] Liu Ct, Lindsay,W. T. ,Jr. Thermodynamics of sodium chloride solutions at high temperatures: The Journal of Solution Chemistry. J.Sol.Chem. 1972;1(1):45–69.
[46] Rogers PSZ, Pitzer KS. Volumetric Properties of Aqueous Sodium Chloride Solutions. J.Phys.Chem.Ref.Data 1982;11(1):15–81.
[47] Harvey AH. Semiempirical correlation for Henry's constants over large temperature ranges. AIChE J. 1996;42:1491–4.
[48] Gerecke J. A contribution to the gas solubility in electrolyte solutions examined using the exemple of the solubility of H2, CO2 and NH3 in water and in aqueous solutions. TH Carl Schorlemmer, Leuna-Merseburg; 1969.
[49] Crozier TE, Yamamoto S. Solubility of hydrogen in water, sea water, and sodium chloride solutions. J. Chem. Eng. Data 1974;19(3):242–4. https://doi.org/10.1021/je60062a007.
[50] Cramer SD. Solubility of methane in brines from 0 to 300.degree.C. Ind. Eng. Chem. Proc. Des. Dev. 1984;23(3):533–8. https://doi.org/10.1021/i200026a021.
[51] Wiebe R, Gaddy VL. The Solubility of Hydrogen in Water at 0, 50, 75 and 100-Ý from 25 to 1000 Atmospheres. J.Am.Chem.Soc. 1934;56(1):76–9. https://doi.org/10.1021/ja01316a022.
[52] Gillespie PC, Wilson GM. Vapor-Liquid Equilibrium Data on Water-Substitute Gas Components: N2-H2O, H2-H2O, CO-H2O, H2-CO-H2O and H2S-H2O. GPA Research Report 1980, 1980.
[53] Chapoy A, Coquelet C, Richon D. Solubility measurement and modeling of water in the gas phase of the methane/water binary system at temperatures from 283.08 to 318.12 K and pressures up to 34.5 MPa. Fluid Phase Equilib. 2003;214(1):101–17.
[54] Appelo CAJ. Principles, caveats and improvements in databases for calculating hydrogeochemical reactions in saline waters from 0 to 200°C and 1 to 1000atm. Applied Geochemistry 2015;55:62–71. https://doi.org/10.1016/j.apgeochem.2014.11.007.

[55] Kunz O, Wagner W. The GERG-2008 Wide-Range Equation of State for Natural Gases and Other Mixtures: An Expansion of GERG-2004. J. Chem. Eng. Data 2012;57(11):3032–91. https://doi.org/10.1021/je300655b.